



**HAL**  
open science

# Modeling of Mixed Cracks in Rock-Like Brittle Materials Under Compressive Stresses by a Double-Phase-Field Method

Zhan Yu, Yue Sun, Minh-Ngoc Vu, Jian-Fu Shao

► **To cite this version:**

Zhan Yu, Yue Sun, Minh-Ngoc Vu, Jian-Fu Shao. Modeling of Mixed Cracks in Rock-Like Brittle Materials Under Compressive Stresses by a Double-Phase-Field Method. *Rock Mechanics and Rock Engineering*, 2022, 56 (4), pp.2779-2792. 10.1007/s00603-022-03196-w . hal-04364474

**HAL Id: hal-04364474**

**<https://hal.science/hal-04364474>**

Submitted on 3 Jan 2024

**HAL** is a multi-disciplinary open access archive for the deposit and dissemination of scientific research documents, whether they are published or not. The documents may come from teaching and research institutions in France or abroad, or from public or private research centers.

L'archive ouverte pluridisciplinaire **HAL**, est destinée au dépôt et à la diffusion de documents scientifiques de niveau recherche, publiés ou non, émanant des établissements d'enseignement et de recherche français ou étrangers, des laboratoires publics ou privés.

# Modelling of mixed cracks in rock-like brittle materials under compressive stresses by a double phase-field method

Zhan YU<sup>a,b</sup>, Yue SUN<sup>b</sup>, Minh-Ngoc VU<sup>c</sup>, Jian-Fu SHAO<sup>a,b,\*</sup>

<sup>a</sup>Key Laboratory of Ministry of Education on Safe Mining of Deep Metal Mines, College of Resources and Civil Engineering, Northeastern University, Shenyang, 110819, China

<sup>b</sup>University of Lille, CNRS, EC Lille, LaMcube, UMR9013, 59000 Lille, France

<sup>c</sup>Andra, Chatenay Malabry, France

---

## Abstract

A new phase-field method is proposed in this paper for modelling complex cracking process in rock-like brittle materials under compression-dominating stresses. For this purpose, two crack fields are introduced in order to respectively describe tensile and shear cracks, related to two independent dissipation processes. The evolution of these fields is described by using the variational principle and thermodynamics framework. The proposed method is implemented in a finite element code and applied to investigating cracking process in a rock-like sample containing two initial flaws and subjected to uniaxial and bi-axial compression. Both tensile wing and shear cracks as well as crack coalescence observed in laboratory tests are successfully reproduced by the proposed method. Differently with most previous studies, the effect of confining stress on shear cracking growth is well described.

*Keywords:* Damage, cracking, crack coalescence, phase-field method, rock-like materials, Compressive stresses

---

## Highlights

- A new phase-field model is developed for modeling complex cracking in rock-like materials under compressive loads.
- Two damage fields are introduced in order to describe tensile and shear cracks.

---

\*Corresponding author: jian-fu.shao@polytech-lille.fr

- A new criterion is proposed for the description of shear crack under multi-axial compression.
- The new model is able to well reproduce complex cracking processes observed in laboratory tests.

## 1. Introduction

In many engineering materials, macroscopic fractures are generally generated by the coalescence of diffuse micro-cracks. The description of transition from diffuse micro-cracks to localized macroscopic fractures is the key issue of modelling failure process in materials and structures. Further, under multi-axial loading conditions, multiple fractures can initiate, propagate and interact. There is a real challenge for numerical modelling. Different methods have been developed during the last decades to deal with this complex subject. For example, enriched finite element methods have been first developed to account for displacement discontinuities along crack surfaces at the elementary level with the help of enriched shape functions [1]. Extended finite element methods (XFEM) have been developed to deal with crack displacement discontinuities by using nodal enrichment techniques [2]. These methods have successfully been applied to different types of materials and structures, in particular hydraulic fracturing in porous rocks [3, 4]. In these two types of methods, the transition from diffuse damage to localized fractures is still a pending issue. The thick level set has been recently proposed to remediate the issue of damage-fracturing transition [5, 6]. The description of multiple cracks in three-dimensional conditions is also a delicate task. On the other hand, based on homogenization techniques, some micro-mechanical models have also been developed for capturing the initiation and growth of micro-cracks and their transition to localized cracks in a representative elementary volume [7, 8, 9]. The efficiency of such models at the structure scale still needs to be demonstrated.

More recently, based on the framework of variational principle for fracture mechanics [10] and the optimal approximations methods of functionals with jumps [11, 12, 13], the so-called phase-field method has been rapidly developed [14]. The sharp topology of crack is

24 approximated by a regularized one which is a non-local function of damage variable and its  
25 gradient (phase-field). The phase-field is determined by a specific boundary values problem.  
26 This approach is particularly suitable to deal with the natural transition from diffuse damage  
27 to localized cracks, interacting multiple cracks and three dimensional problems. Different  
28 extensions have been proposed for various purposes, dynamic brittle fracture [15], fast com-  
29 puting with a new hybrid formulation [16], multi-physics problems [17], finite deformation  
30 [18], and coupling between damage and plasticity [19, 20], etc..

31 In most previous studies, the accent was put on tensile cracks which are driven by  
32 the elastic strain energy related to tensile eigenvalues. As in a wide range of engineering  
33 structures, shear cracks are also an important mechanism, different extensions have been  
34 proposed in some recent works. For instance in [21, 22], the authors have proposed a  
35 specific decomposition of the ratio between driving strain energy and critical fracture energy  
36 into a tensile part (mode I) and a shear part (mode II). The phase-field evolution is thus  
37 driven by both the tensile and shear strain energy. And each part is controlled by a critical  
38 fracture energy (mode I and mode II). The efficiency of this method in modelling mixed crack  
39 propagation has been demonstrated. More recently, in [23], the concept of multiple phase-  
40 field has been introduced to describe the damage accumulation in different cleavage planes  
41 of polycrystalline materials. Similarly, this type of concept has been applied to anisotropic  
42 materials in order to capture different cracking patterns in [24]. However, those previous  
43 studies have mainly focused on tensile and shear loads.

44 Most rock-like materials are subjected to compression-dominating stresses. Crack initia-  
45 tion and propagation in these materials subjected to compressive loads exhibit complex and  
46 mixed patterns [25, 26], such as compression-induced tensile wing and shear cracks. Further,  
47 the mechanical behavior of rock-like materials is strongly dependent on compressive mean  
48 stress. For instance, the shear crack growth is directly affected by the compressive normal  
49 stress. For this purpose, a phase-field model for compressive-shear fracture was proposed  
50 by introducing a hybrid approach in [27]. Moreover, based on the assumption of frictional  
51 contact [28] and friction energy [29], some authors proposed a frictional fracture phase-field  
52 model [30] and a mixed-FE scheme [31] to deal with compression-induced shear cracks in

53 rock-like materials. On the other hand, the phase-field model for mixed-mode fracture were  
54 introduced in [32, 33]. Further, some authors focused on the compressive-ductile behavior  
55 of mixed-mode phase-field model by considering micro-structure [34, 35].

56 The so-called multi phase-field were firstly proposed and applied on polycrystal [36].  
57 The conception of “multi” is introduced to describe the anisotropy of damage on cleavage  
58 planes. The same conception is also used in the most work of multi phase-field [37, 38, 39].  
59 Conversely, it is worth to note that the conception of the double phase-field is different from  
60 that of the multi phase-field, even if they have a similar call. The principal feature of double  
61 phase-field method is the use of two damage variables (or more than two if necessary). This  
62 conception is firstly appeared in the study of [40], the two damage variables is introduced to  
63 identify the different effect of longitudinal and transverse failure for anisotropic materials.  
64 For a different purpose, [41] proposed a double phase-field with the damage variables defined  
65 as tensile damage and shear damage, which are driven by the energy decomposed according  
66 to the strain state. Similarly, [42] proposed a double phase-field method to consider the  
67 tensile and compressive-shear crack. The onset/effect of tensile crack and compressive-shear  
68 crack are according to crack conditions of “open”, “stick” and “slip”. The two types of crack  
69 are identified based on a complex calculation due to the stress in the direction perpendicular  
70 and parallel to the interface of the crack.

71 In the present study, a new phase-field method is proposed for modelling mixed cracks  
72 in rock-like brittle materials subjected to compression-dominating stresses. Two phase-field  
73 variables are introduced to describe the tensile and compressive-shear cracks respectively.  
74 Mixed cracks can be represented by the combination of these two phase-field variables by  
75 using a spectral decomposition of stress. Different from the work of [41], the tensile and  
76 compressive crack are distinguished by stat of stress instead of strain in order to adopt  
77 the rock-like material. Furthermore, with a same purpose of [42], by using a more sim-  
78 ply and also reasonable way, a modified Morh-Coulomb criterion is introduced to identify  
79 the compressive-shear crack, which is more suitable to consider the properties of internal  
80 friction and cohesion for rock-like material. Another way to deal with the issue of mixed  
81 crack is provided. The efficiency of the proposed method is assessed through comparisons

82 between numerical results and experimental evidence. It is shown that different types of  
 83 crack propagation scenarios can be well described by the proposed method.

## 84 **2. A double phase-field method**

### 85 *2.1. Regularized crack density*

86 We consider here a solid body occupying the volume  $\Omega$ , subjected to the body force  $\mathbf{f}_b$  in  
 87  $\Omega$ , the surface force  $\mathbf{t}_N$  on its external boundary  $\partial\Omega_f$  and the prescribed displacement  $\bar{\mathbf{u}}$  on  
 88 its **external** boundary  $\partial\Omega_u$ . Due to the applied loads, there is initiation and propagation of  
 89 cracks. In the case of rock like materials under compression-dominating stresses, complex  
 90 cracking processes have been observed [43, 44, 45]. In general, three types of cracks, namely  
 91 tensile, shear and mixed, can initiate and propagate depending on loading path and material  
 92 microstructure. Under direct tension or in triaxial extension conditions, tensile cracks repre-  
 93 sent the main process. Under triaxial compression conditions, in particular when confining  
 94 stress is high, frictional shear cracks are the dominant mechanism. In general loading con-  
 95 ditions, mixed cracks can be generated by combined tensile and shear strains or stresses. In  
 96 order to conveniently describe such complex cracking processes, two independent crack fields  
 97 are here introduced to respectively represent the tensile and shear cracks. Mixed cracks are  
 98 then described by the combination of these two fields.

99 In the framework of phase-field method, the real crack surface area is approximated by  
 100 the regularized one [14]. By considering the two crack fields, the total regularized crack  
 101 surface area  $\Gamma_{l_d}$  is expressed as follows:

$$\Gamma_{l_d} = \Gamma_{l_d}^t(d^t) + \Gamma_{l_d}^s(d^s) = \int_{\Omega} \{\gamma^t(d^t, \nabla d^t) + \gamma^s(d^s, \nabla d^s)\} dV \quad (1)$$

102 where  $\Gamma_{l_d}^\alpha$  ( $\alpha = t, s$ ) are the contributions of tensile and shear cracks to the total crack  
 103 surface area. Two scalar-valued functions  $\gamma^\alpha(d^\alpha, \nabla d^\alpha)$  denote the tensile and shear crack  
 104 density (surface area per unit volume). There are different forms available to define the  
 105 crack surface density  $\gamma^\alpha$ . A common form was introduced in [11] and it is adopted here:

$$\gamma^\alpha(d^\alpha, \nabla d^\alpha) = \frac{1}{2l_d}(d^\alpha)^2 + \frac{l_d}{2}\nabla d^\alpha \cdot \nabla d^\alpha \quad ; \quad \alpha = t, s \quad (2)$$

106 In these functions, a scalar-valued variable  $d^\alpha(\mathbf{x})$  ( $\alpha = t, s$ ) is introduced for each type of  
 107 crack and it is conventionally called the phase-field (or crack) variable. It is worth noticing  
 108 that the crack surface density  $\gamma^\alpha$  is a function of  $d^\alpha$  and its gradient  $\nabla d^\alpha$ .  $l_d$  is a length  
 109 scale parameter controlling the width of regularized smeared crack surfaces. This non-  
 110 local property allows the phase-field method to avoid the pathologic mesh dependency of  
 111 numerical solution. Further, the value of  $d^\alpha(\mathbf{x})$  ( $\alpha = t, s$ ) also indicate the current damage  
 112 state of material, more precisely  $d^\alpha(\mathbf{x}) = 0$  being the sound state while  $d^\alpha(\mathbf{x}) = 1$  the fully  
 113 damaged one as shown in Figure 1.

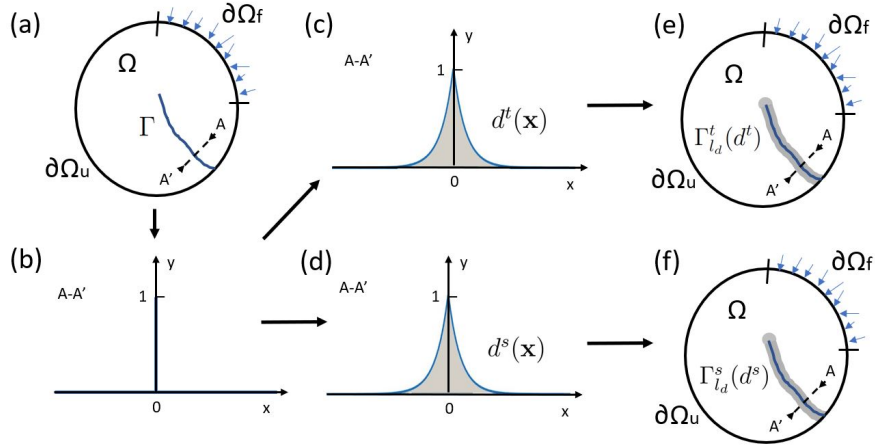


Figure 1: (a) A sharp crack  $\Gamma$  inside solid body  $\Omega$ ; (b) auxiliary damage variable in sharp crack topology along the 1D line  $A-A'$ ; (c) and (d) tensile and shear crack phase-field in regularized crack topology along the 1D line  $A-A'$ ; (e) and (f) regularized representation of tensile and shear cracks with equivalent crack surfaces  $\Gamma(d^t)$  and  $\Gamma(d^s)$

114 Further, according to the Griffith theory of linear fracture mechanics, the energy needed  
 115 for the creation of a crack surface area is characterized by the material toughness or fracture  
 116 energy. With the regularized smooth representation of cracks adopted here, one can express  
 117 the energy density per unit volume needed for the creation of tensile and shear cracks as  
 118 follows:

$$w_c(d^t, d^s, \nabla d^t, \nabla d^s) = g_c^t \gamma^t(d^t, \nabla d^t) + g_c^s \gamma^s(d^s, \nabla d^s) \quad (3)$$

119  $g_c^t$  and  $g_c^s$  denotes the material toughness for the tensile and shear crack respectively.

120 *2.2. Variational framework*

121 According to the variational approach to fracture mechanics of elastic materials proposed  
 122 in [10], under the isothermal conditions, the total energy functional of a solid domain  $\Omega$  is  
 123 composed of the elastic strain energy and that requested to create the cracks, with the  
 124 regularized crack fields adopted above, one gets:

$$E(\boldsymbol{\epsilon}, d^t, d^s) = \int_{\Omega} w_e(\boldsymbol{\epsilon}, d^t, d^s) dV + \int_{\Omega} w_c dV \quad (4)$$

125  $w_e$  is the elastic strain energy density of cracked material.  $\boldsymbol{\epsilon}(\mathbf{u})$  denotes the second order  
 126 linear strain tensor with  $\mathbf{u}(\mathbf{x})$  being the displacement vector such as  $\boldsymbol{\epsilon} = \nabla^s \mathbf{u}$ .

127 *2.2.1. Elastic strain energy*

128 In the present study, two crack fields are introduced and affect differently the elastic strain  
 129 energy. In order to better describe the coupling between the cracking processes and elastic  
 130 properties of cracked material, the elastic strain energy of undamaged solid is decomposed  
 131 into a tensile part  $w_{e+}^0$  and a compressive part  $w_{e-}^0$ :

$$w_e^0(\boldsymbol{\epsilon}) = w_{e+}^0(\boldsymbol{\epsilon}) + w_{e-}^0(\boldsymbol{\epsilon}) = \frac{1}{2} \boldsymbol{\sigma}^+ : \boldsymbol{\epsilon} + \frac{1}{2} \boldsymbol{\sigma}^- : \boldsymbol{\epsilon} \quad (5)$$

132 Two symmetric tensors  $\boldsymbol{\sigma}^{\pm}$  denote the tensile and compressive parts of the Cauchy stress  
 133 tensor  $\boldsymbol{\sigma}$ , and they are calculated by using the following fourth order projection operators  
 134  $\mathbb{P}_{\sigma}^{\pm}$  :

$$\begin{cases} \boldsymbol{\sigma}_+ = \mathbb{P}_{\sigma}^+ : \boldsymbol{\sigma} \\ \boldsymbol{\sigma}_- = \mathbb{P}_{\sigma}^- : \boldsymbol{\sigma} \end{cases} \quad (6)$$

135 These operators are further constructed from the spectral decomposition of the stress tensor  
 136 proposed in [46, 47]:

$$\begin{cases} \mathbb{P}_{\sigma}^+ = \sum_{\beta=1}^3 \langle \sigma^{\beta} \rangle_+ \mathbf{n}^{\beta} \otimes \mathbf{n}^{\beta} \otimes \mathbf{n}^{\beta} \otimes \mathbf{n}^{\beta} \\ \mathbb{P}_{\sigma}^- = \mathbb{I} - \mathbb{P}_{\sigma}^+ \end{cases} \quad (7)$$

137  $\mathbb{I}$  denotes the fourth-order identity tensor.  $\mathbf{n}^{\beta} (\beta = 1, 2, 3)$  define the three orthogonal  
 138 principal directions of the stress tensor while  $\sigma^{\beta}$  are the three principal stresses. The bracket



139  $\langle \cdot \rangle_+$  is defined as:

$$\begin{cases} \langle a \rangle_+ = a, & a \geq 0 \\ \langle a \rangle_+ = 0, & a < 0 \end{cases} \quad (8)$$

140 It is worth noticing that the projection operators are widely used for the decomposition  
 141 of stress or strain tensor into tensile and compressive parts, including some previous phase-  
 142 field models [48, 49, 50]. In general, even for elastically isotropic materials, the projection  
 143 operators for stress  $\mathbb{P}_\sigma$  and for strain  $\mathbb{P}_\epsilon$  are different. As in the previous work [50], the de-  
 144 composition of stress tensor is adopted here. Compared with the strain tensor decomposition  
 145 as that used in [14], the stress decomposition avoids the implication of elastic parameters.  
 146 It is particularly convenient for future extension to initial anisotropic materials.

147 The elastic properties of cracked material are affected by the growth of cracks. This is  
 148 generally described by introducing different forms of degradation functions. In the present  
 149 study, two degradation functions are defined respectively for the tensile and shear cracks.  
 150 The elastic strain energy of cracked material is expressed as follows:

$$w_e(\boldsymbol{\epsilon}, d^t, d^s) = h_t(d^t)w_{e+}^0 + h_s(d^s)w_{e-}^0 \quad (9)$$

151 The common form widely used in previous studies [48, 49, 50] is adopted here for the two  
 152 degradation functions:

$$h_\alpha(d^\alpha) = (1 - d^\alpha)^2(1 - k) + k; \quad \alpha = t, s \quad (10)$$

153  $k$  is a small positive value that is used to ensure the positive definiteness of elastic stiffness  
 154 tensor after the material is fully broken ( $d^\alpha = 1$ ).

### 155 2.2.2. Governing equations of crack fields

156 Based on the expressions of  $w_e$  and  $w_c$  defined above, the total energy functional  $E$  can  
 157 be detailed in the following form:

$$\begin{aligned} E &= \int_{\Omega} w_e(\boldsymbol{\epsilon}, d^t, d^s) dV + \int_{\Omega} w_c(d^t, d^s, \nabla d^t, \nabla d^s) dV \\ &= \int_{\Omega} \{h_t(d^t)w_{e+}^0 + h_s(d^s)w_{e-}^0\} dV + \int_{\Omega} \{g_c^t \gamma^t(d^t, \nabla d^t) + g_c^s \gamma^s(d^s, \nabla d^s)\} dV \end{aligned} \quad (11)$$

158 We assume that the growths of tensile and shear cracks are two independent dissipation  
159 processes. Each of them verifies the positiveness condition independently. Further, inspired  
160 by the previous studies [51, 52], each crack field can be determined by solving the minimiza-  
161 tion problem of the energy functional  $E$ . By calculating the first order variation of  $E$  and  
162 using the unilateral stationary condition for the total energy functional with respect to each  
163 crack variable, namely  $\delta E = 0$  for  $\delta d^\alpha > 0$  and  $\delta E > 0$  for  $\delta d^\alpha = 0$  ( $\alpha = t, s$ ), the following  
164 governing equations for the evolution of two crack fields ( $\alpha = t, s$ ) can be derived:

$$\begin{cases} -\frac{\partial w_e}{\partial d^\alpha} - g_c^\alpha \delta_{d^\alpha} \gamma^\alpha = 0 & , \quad \dot{d}^\alpha > 0 & , \quad \text{in } \Omega \\ -\frac{\partial w_e}{\partial d^\alpha} - g_c^\alpha \delta_{d^\alpha} \gamma^\alpha \leq 0 & , \quad \dot{d}^\alpha = 0 & , \quad \text{in } \Omega \\ \frac{\partial \gamma}{\partial \nabla d^\alpha} \cdot \mathbf{n} = 0 & , \quad \text{on } \delta\Omega \end{cases} \quad (12)$$

165 where  $\delta_{d^\alpha} \gamma^\alpha = \frac{\partial \gamma^\alpha}{\partial d^\alpha} - \text{div} \left( \frac{\partial \gamma^\alpha}{\partial \nabla d^\alpha} \right)$  denotes the variational derivative of crack field  $d^\alpha$  [51, 52].  
166 By substituting  $w_e$  and  $\gamma^\alpha$  by their specific forms presented above, one obtains the governing  
167 equations for two crack fields as follows:

$$\begin{cases} -h'_t(d^t)w_{e+}^0 - g_c^t \left\{ \frac{1}{l_d} d^t - l_d \text{div}(\nabla d^t) \right\} = 0 & , \quad \dot{d}^t > 0 \\ -h'_s(d^s)w_{e-}^0 - g_c^s \left\{ \frac{1}{l_d} d^s - l_d \text{div}(\nabla d^s) \right\} = 0 & , \quad \dot{d}^s > 0 \end{cases} \quad (13)$$

168 where  $h'_t(d^t) = -2(1-k)(1-d^t)$  and  $h'_s(d^s) = -2(1-k)(1-d^s)$  are the derivatives of two  
169 degradation functions with respect to two damage variables.

170 From the threshold function (13)(b), it is observed that the evolution of the shear crack  
171  $d^s$  is driven by the compressive part of the elastic strain energy associated with the intact  
172 state  $w_{e-}^0$ . This is physically not fully justified. In practice, for most rock-like materials  
173 under compressive stresses, the shear crack is physically controlled by a generalized shear  
174 stress. The later can be well represented by the shear force defined by the widely used  
175 Mohr-Coulomb criterion. Based on this physical background and inspired by some previous  
176 studies [53, 27], an alternative driving energy  $w^s$  is defined as follows for the description of  
177 shear crack growth:

$$w^s(\boldsymbol{\sigma}) = \frac{1}{2G} \left\langle \frac{\sigma_1 - \sigma_3}{2 \cos \varphi} + \frac{\sigma_1 + \sigma_3}{2} \tan \varphi - c \right\rangle_+^2 \quad (14)$$

178 In this relation,  $\sigma_1$  and  $\sigma_3$  are the major and minor principal stress respectively.  $G$  is  
 179 the initial shear modulus of intact material.  $\varphi$  denotes the internal friction angle and  $c$  the  
 180 cohesion. Moreover, it is assumed that the shear crack growth occurs only in the compressive  
 181 domain of principal stresses. Therefore, the driving energy of shear crack growth corresponds  
 182 to the compressive part of  $w^s$ , which is defined as:

$$w_-^s(\boldsymbol{\sigma}^-) = \frac{1}{2G} \left\langle \frac{\langle \sigma_1 \rangle_- - \langle \sigma_3 \rangle_-}{2 \cos \varphi} + \frac{\langle \sigma_1 \rangle_- + \langle \sigma_3 \rangle_-}{2} \tan \varphi - c \right\rangle_+^2 \quad (15)$$

183 with the bracket  $\langle \cdot \rangle_-$  defining:

$$\begin{cases} \langle a \rangle_- = 0, & a \geq 0 \\ \langle a \rangle_- = a, & a < 0 \end{cases} \quad (16)$$

184 By substituting the physically-based driving energy for the compressive shear crack  
 185 growth for (13), the new criteria for two crack fields is expressed as:

$$\begin{cases} -h'_t(d^t)w_{e+}^0 - g_c^t \left\{ \frac{1}{l_d} d^t - l_d \operatorname{div}(\nabla d^t) \right\} = 0, & \dot{d}^t > 0 \\ -h'_s(d^s)w_-^s - g_c^s \left\{ \frac{1}{l_d} d^s - l_d \operatorname{div}(\nabla d^s) \right\} = 0, & \dot{d}^s > 0 \end{cases} \quad (17)$$

186 On the other hand, in order to describe the irreversible process of crack growth in general  
 187 loading paths with unloading and reloading cycles, the concept of loading history functional  
 188 has been introduced in [54]. Based on that concept, two energy history functionals are here  
 189 defined as follows for the grow description of tensile and shear cracks:

$$\begin{cases} \mathcal{H}^t = \max[w_{e+}^0(\boldsymbol{\sigma}^+, \tau)]_{\tau \in [0, t]} \\ \mathcal{H}_-^s = \max[w_-^s(\boldsymbol{\sigma}^-, \tau)]_{\tau \in [0, t]} \end{cases} \quad (18)$$

190 The time variable  $\tau$  designates the loading history from the initial state to the current time  
 191 step  $t$ . Using these energy history functionals, the evolution of the tensile and shear crack  
 192 is determined by the following criteria:

$$\begin{cases} -h'_t(d^t)\mathcal{H}^t - g_c^t \left\{ \frac{1}{l_d} d^t - l_d \operatorname{div}(\nabla d^t) \right\} = 0 \\ -h'_s(d^s)\mathcal{H}_-^s - g_c^s \left\{ \frac{1}{l_d} d^s - l_d \operatorname{div}(\nabla d^s) \right\} = 0 \end{cases} \quad (19)$$

### 193 3. Numerical implementation with finite element method

194 The problem to be solved here consists in the determination of displacement field  $\mathbf{u}(\mathbf{x})$ ,  
 195 the tensile crack field  $d^t(\mathbf{x})$  and the shear crack field  $d^s(\mathbf{x})$ , at each loading step and with the  
 196 boundary conditions defined above. For this purpose, the total potential energy is expressed  
 197 as:

$$\Pi = E(\mathbf{u}, d^t, d^s) - \int_{\Omega} \mathbf{f}_b \cdot \mathbf{u} d\Omega - \int_{\partial\Omega_f} \mathbf{t}_N \cdot \mathbf{u} dA \quad (20)$$

198 The stationarity condition of the potential energy  $\delta\Pi = 0$  leads to three coupled systems of  
 199 equations to be solved in terms of the displacement, the tensile crack and the shear crack  
 200 fields respectively. However, due to the growth of cracks, it is needed to solve a strongly  
 201 non-linear problem. For this purpose, the whole loading path is divided into a number of  
 202 increments or time steps. Starting from the initial known values of all physical quantities, at  
 203 the end of loading step  $i$ , the values of  $\mathbf{u}(\mathbf{x}, t_i)$ ,  $d^t(\mathbf{x}, t_i)$  and  $d^s(\mathbf{x}, t_i)$  are assumed to be known.  
 204 During the loading step  $t_{t+1} = t_i + \Delta t_{t+1}$ , the solutions to be determined are the increments  
 205 of three principal unknowns, namely  $\Delta\mathbf{u}(\mathbf{x}, \Delta t_{t+1})$ ,  $\Delta d^t(\mathbf{x}, \Delta t_{t+1})$  and  $\Delta d^s(\mathbf{x}, \Delta t_{t+1})$ .

206 The finite element method is adopted in the present work. Based on the geometrical  
 207 discretization and with the help of the shape functions and their derivatives for the type of  
 208 element adopted, one obtains three discrete systems of equations to be solved.

209 For the mechanical problem, the Cauchy stress tensor  $\boldsymbol{\sigma}$  verifies the following equilibrium  
 210 equations:

$$\begin{cases} \nabla \cdot \boldsymbol{\sigma} + \mathbf{f}_b = 0 & \text{in } \Omega \\ \boldsymbol{\sigma} \cdot \mathbf{n} = \mathbf{t}_N & \text{on } \partial\Omega_t \end{cases} \quad (21)$$

211 The constitutive relation of cracked material is defined by:

$$\boldsymbol{\sigma} = \mathbb{C}(d^t, d^s) : \boldsymbol{\epsilon} \quad ; \quad \mathbb{C}(d^t, d^s) = h_t(d^t)\mathbb{P}_{\sigma}^+ : \mathbb{C}^0 + h_s(d^s)\mathbb{P}_{\sigma}^- : \mathbb{C}^0 \quad (22)$$

212 where  $\mathbb{C}^0$  is the elastic stiffness matrix of intact material. Together with the kinematic  
 213 relation  $\boldsymbol{\epsilon} = \nabla^s \mathbf{u}$ , the discrete system of equations of the mechanical problem is given by:

$$\begin{cases} \mathbf{K}^u \Delta \mathbf{U} = \Delta \mathbf{F} \\ \mathbf{K}^u = \int_{\Omega} \mathbf{B}_u^T \mathbb{C} \mathbf{B}_u d\Omega \\ \Delta \mathbf{F} = \int_{\Omega} \mathbf{N}_u^T \Delta \mathbf{f}_b d\Omega + \int_{\partial\Omega_f} \mathbf{N}_u^T \Delta \mathbf{t}_N dA \end{cases} \quad (23)$$

214  $\mathbf{N}_u$  and  $\mathbf{B}_u$  are respectively the matrix of shape functions and related derivatives of dis-  
 215 placement components.  $\mathbf{K}^u$  is the global stiffness matrix.  $\Delta\mathbf{U}$  and  $\Delta\mathbf{F}$  denote the column  
 216 matrices of increment nodal displacements and forces during the current loading step (for  
 217 the sake of simplicity, the step index  $i + 1$  is here omitted).

218 On the other hand, with the crack growth criteria (19) in hand, the tensile crack phase-  
 219 field is determined by the following local equations:

$$\begin{cases} h'_t(d^t)\mathcal{H}^t + g_c^t \left\{ \frac{1}{l_d}d^t - l_d \text{div}(\nabla d^t) \right\} = 0 & \text{in } \Omega \\ \dot{d}^t \geq 0 & \text{in } \Omega \\ d^t = 1 & \text{on } \Gamma^t \\ \nabla d^t \cdot \mathbf{n} = 0 & \text{on } \partial\Omega \end{cases} \quad (24)$$

220 while the shear crack phase-field is described by the following ones:

$$\begin{cases} h'_s(d^s)\mathcal{H}_-^s + g_c^s \left\{ \frac{1}{l_d}d^s - l_d \text{div}(\nabla d^s) \right\} = 0 & \text{in } \Omega \\ \dot{d}^s \geq 0 & \text{in } \Omega \\ d^s = 1 & \text{on } \Gamma^s \\ \nabla d^s \cdot \mathbf{n} = 0 & \text{on } \partial\Omega \end{cases} \quad (25)$$

221 The same geometrical mesh is used for the phase-field problems as for the mechanical  
 222 one. Further, as for the displacement field, the two crack fields and their gradients inside  
 223 each element are also approximated in terms of by the nodal values by using appropriate  
 224 shape functions and related derivatives. With such approximations, the following discrete  
 225 systems of equations are obtained for each crack phase-field. Namely, for the tensile cracks  
 226 field, one gets:

$$\begin{cases} \mathbf{K}^{d^t} \mathbf{d}^t = \mathbf{F}^{d^t} \\ \mathbf{K}^{d^t} = \int_{\Omega} \{ (g_c^t/l_d + 2\mathcal{H}^t) \mathbf{N}_d^T \mathbf{N}_d + g_c^t l_d \mathbf{B}_d^T \mathbf{B}_d \} d\Omega \\ \mathbf{F}^{d^t} = \int_{\Omega} 2\mathcal{H}^t \mathbf{N}_d^T d\Omega \end{cases} \quad (26)$$

227 and for the shear crack field:

$$\begin{cases} \mathbf{K}^{d^s} \mathbf{d}^s = \mathbf{F}^{d^s} \\ \mathbf{K}^{d^s} = \int_{\Omega} \{ (g_c^s/l_d + 2\mathcal{H}_-^s) \mathbf{N}_d^T \mathbf{N}_d + g_c^s l_d \mathbf{B}_d^T \mathbf{B}_d \} d\Omega \\ \mathbf{F}^{d^s} = \int_{\Omega} 2\mathcal{H}_-^s \mathbf{N}_d^T d\Omega \end{cases} \quad (27)$$

228  $\mathbf{N}_d$  and  $\mathbf{B}_d$  are the matrices of shape functions and related derivatives for the approximation  
 229 of two crack phase-fields.  $\mathbf{K}^{d^\alpha}$  ( $\alpha = t, s$ ) is the global stiffness matrix related to the tensile  
 230 or shear crack field.  $\mathbf{F}^{d^\alpha}$  denotes the column matrix of nodal forces while  $\mathbf{d}^\alpha$  that of nodal  
 231 damage variables at the current loading step (for the sake of simplicity, the step index  $i + 1$   
 232 is here omitted). It is worth noticing that with the help of two energy history functionals  
 233 defined in (18), the values of damage variables at the current loading step are directly  
 234 determined as functions of the accumulated driving energy for each cracking mechanisms.

235 It is obvious that three fields are strongly coupled. The calculation of displacement field  
 236 is influenced by the crack phase-fields due to the fact that the elastic stiffness matrix of  
 237 cracked material  $\mathbb{C}(\mathbf{x})$  is a function of two crack fields  $d^t(\mathbf{x})$  and  $d^s(\mathbf{x})$ . Inversely, the growth  
 238 of both tensile and shear cracks is controlled by the mechanical energy which is related to  
 239 the variation of displacement field.

240 In this way, the so-called Alternate Minimization (AM) solver proposed in [13, 55] is  
 241 used in this work because of its good robustness performance. At the iteration  $k + 1$  of the  
 242 loading step  $n + 1$ , two solution stages are summarized as:

243 Stage 1:

$$\mathbf{K}^u(\mathbb{C})\Delta\mathbf{U}_{n+1}^{k+1} = \Delta\mathbf{F}_{n+1}, \text{ with } \mathbb{C} = \mathbb{C}([d^t, d^s]_{n+1}^k) \quad (28)$$

244 -Solving the displacement  $\Delta\mathbf{U}_{n+1}^{k+1}$  by using the damage values fixed  $[d^t, d^s]_{n+1}^k$  obtained from  
 245 the last iteration  $k$ .

246 Stage 2:

$$\begin{cases} \mathbf{K}^{d^t}(\mathcal{H}^t)[\mathbf{d}^t]_{n+1}^{k+1} = \mathbf{F}^{d^t}(\mathcal{H}^t), \text{ with } \mathcal{H}^t = \mathcal{H}^t(U_{n+1}^{k+1}) \\ \mathbf{K}^{d^s}(\mathcal{H}^s)[\mathbf{d}^s]_{n+1}^{k+1} = \mathbf{F}^{d^s}(\mathcal{H}^s), \text{ with } \mathcal{H}^s = \mathcal{H}^s(U_{n+1}^{k+1}) \end{cases} \quad (29)$$

247 -Solving the damage values  $[d^t, d^s]_{n+1}^{k+1}$  by using the updated displacement  $\mathbf{U}_{n+1}^{k+1}$  obtained  
 248 from the same iteration.

249 The two steps are repeated until the condition  $\| \max([d^t]_{n+1}^{k+1} - [d^t]_{n+1}^k, [d^s]_{n+1}^{k+1} - [d^s]_{n+1}^k) \| \leq R$   
 250 is satisfied, with  $R = 1 \times 10^{-5}$  being used in this work.

## 251 4. Experimental verification

252 In this section, the efficiency of the proposed double phase-field method, in particular  
253 its capability to describe complex cracking patterns under compression-dominating loads is  
254 verified, through the comparison between numerical results and experimental observations.

### 255 4.1. Uniaxial compression of a plate with two inclined flaws

256 In this example, a representative laboratory test is investigated. Uniaxial compression is  
257 performed on a rectangular thin plate containing two initial inclined flaws, as illustrated in  
258 Figure 2. Different configurations of the initial flaws can be considered. More details about  
259 the testing procedures can be found in [56, 57]. This type of test is particularly relevant  
260 for the characterization of complex failure process in brittle materials, including tensile,  
261 shear and mixed cracks and their bridging. The proposed double phase-field method is now  
262 applied to capturing such cracking patterns.

263 The geometry of the plate and the prescribed boundary conditions are presented in Figure  
264 2. The length of two initial flaws is  $2a=12.7\text{mm}$  and their width is  $0.1\text{mm}$ . The configuration  
265 of two flaws is defined in terms of the combination “flaw angle-spacing-continuity”. For  
266 example, the case of “45-a-2a” corresponds to the configuration of two flaws inclined with  
267 an angle of  $\alpha = 45^\circ$ , spaced by  $s = a$  and  $c = 2a$ . In this study, three configurations are  
268 considered, namely “45-0-2a”, “45-a-2a” and “45-2a-2a” are selected for simulation. The  
269 values of mechanical parameters involved on the proposed model are selected mainly from  
270 previous studies [56, 57]. The set of values is given in Table 1. Therefore,  $l_d$  is assumed  
271 as a pure numerical parameter of the regularized model of brittle fracture which depends  
272 on element size  $h$ :  $h < l_d/2$  [54]. In this work, we define  $l_d = 2.5h$  for both of the tensile  
273 and shear damage field.  $h_r$  is the size of the refined element which are assigned to the  
274 region expected to have the propagation of cracks for the sake of computational efficiency.  
275 Following the study of [58],  $g_c^t/l_d$  is considered as a real material parameter, which depends  
276 on stiffness and strength:  $\sigma_c = \frac{3}{16}\sqrt{\frac{3}{2}}\sqrt{\frac{Eg_c^t}{l_d}}$ .  $g_c^s$  is calibrated according to the calculated  
277 toughness value of tensile crack:  $g_c^s=5g_c^t$ .

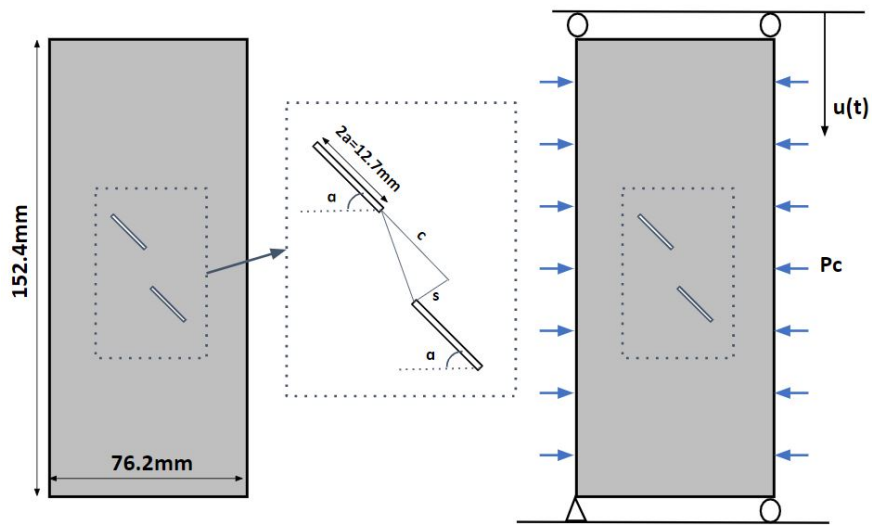


Figure 2: Geometry of plate, configuration of initial flaws and boundary conditions for uniaxial ( $P_c = 0$ ) and bi-axial compression tests ( $P_c = 7.5\text{MPa}$ )



Table 1: Parameter values used in simulations of two inclined flaws test

Elastic parameters:	
E (GPa)	5.96
$\nu$ (-)	0.24
Crack fields parameters:	
$\sigma_c$ (MPa)	3.2
$\varphi$ ( $^\circ$ )	30
$c$ (MPa)	1
$g_c^t$ (kN/mm)	$4.2 \times 10^{-6}$
$g_c^s$ (kN/mm)	$21 \times 10^{-6}$
$l_d$ (mm)	0.25
$k$ (-)	$1 \times 10^{-9}$
Mesh:	
$h_r$ (mm)	0.1
Element number	Around 300,000
Node number	Around 300,000
Displacement increment:	
$\Delta u$ (mm)	$1 \times 10^{-3}$

278 In Figure 3, one shows the distributions of tensile and shear damage ( $d^t$  and  $d^s$ ) for  
 279 the case of “45-0-2a” at six subsequent values of prescribed axial displacement. The red  
 280 color shows the tensile crack and the blue color shows the shear one. In order to investigate  
 281 the cracking patterns more clearly, only the crack with the damage value higher than 0.5  
 282 is shown. Further, for the purpose of comparison, the main crack patterns observed in the  
 283 laboratory test and reported in [56, 57] are illustrated in the same Figure. It is seen that from  
 284 loading step (a) to (b), two external wing cracks and two internal wing cracks are generated  
 285 from the ends of the initial flaws and they propagate towards the axial compression direction.  
 286 These wing cracks are all induced by the tensile damage. At the loading step (c) and (d),

287 the wing cracks continue propagating in the axial direction while one shear damage band is  
288 generated from the two internal ends of the initial flaws. With the increasing of compression  
289 up to step (e) and (f), two external shear cracks are created from the two external ends of  
290 the initial flaws. And the internal shear damage band induces a sharp mixed crack which is  
291 located at the same position. All these features obtained from the numerical results match  
292 very well the experimental evidence.

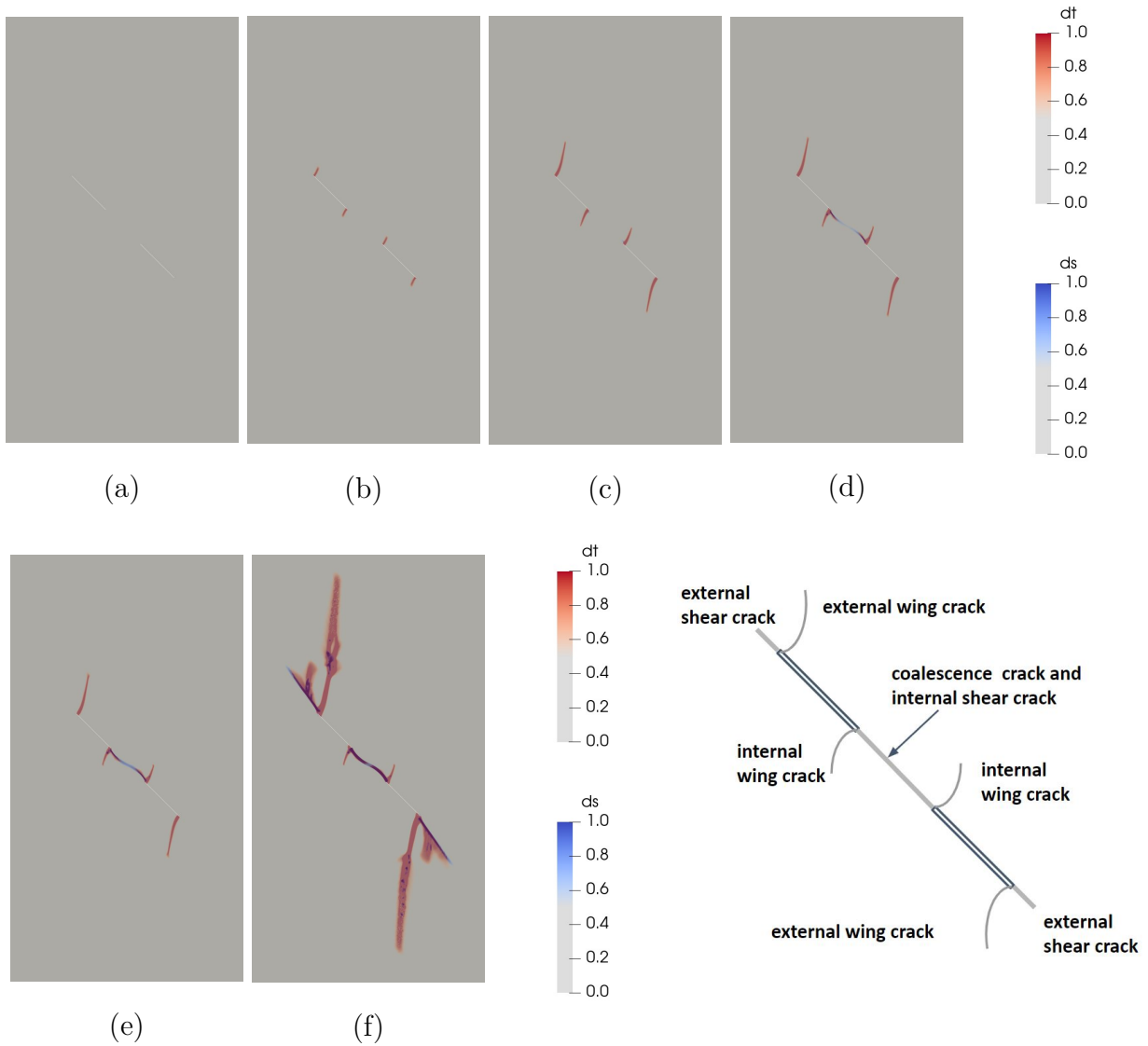


Figure 3: Distribution of tensile and shear damage for the configuration 45-0-2a at three subsequent values of axial displacement (a)  $u = 0$  mm; (b)  $u = 0.620$  mm; (c)  $u = 0.633$  mm; (d)  $u = 0.635$  mm; (e)  $u = 0.30$  mm; (f)  $u = 0.666$  mm

293 The results for the case of “45-a-2a” are presented in Figure 4. Four tensile wing cracks  
 294 appear from the ends of initial flaws and propagate steadily toward the axial direction with  
 295 the increase of compression. The shear cracks are also generated from the external and  
 296 internal ends of initial flaws, but they propagate almost along the prolongation direction of  
 297 the initial flaws. Due to the fact that the two initial flaws are not aligned ( $s = 2a$ ), the two

298 internal shear cracks cannot connect each other along a straight line. As a consequence, the  
 299 coalescence between the tips of two internal shear cracks emerges along a curved path by  
 300 the generation of a mixed crack which propagates towards the axial compression direction.  
 301 Again, all these complex cracking patterns observed in the laboratory test are well captured  
 302 by the double phase-field model.

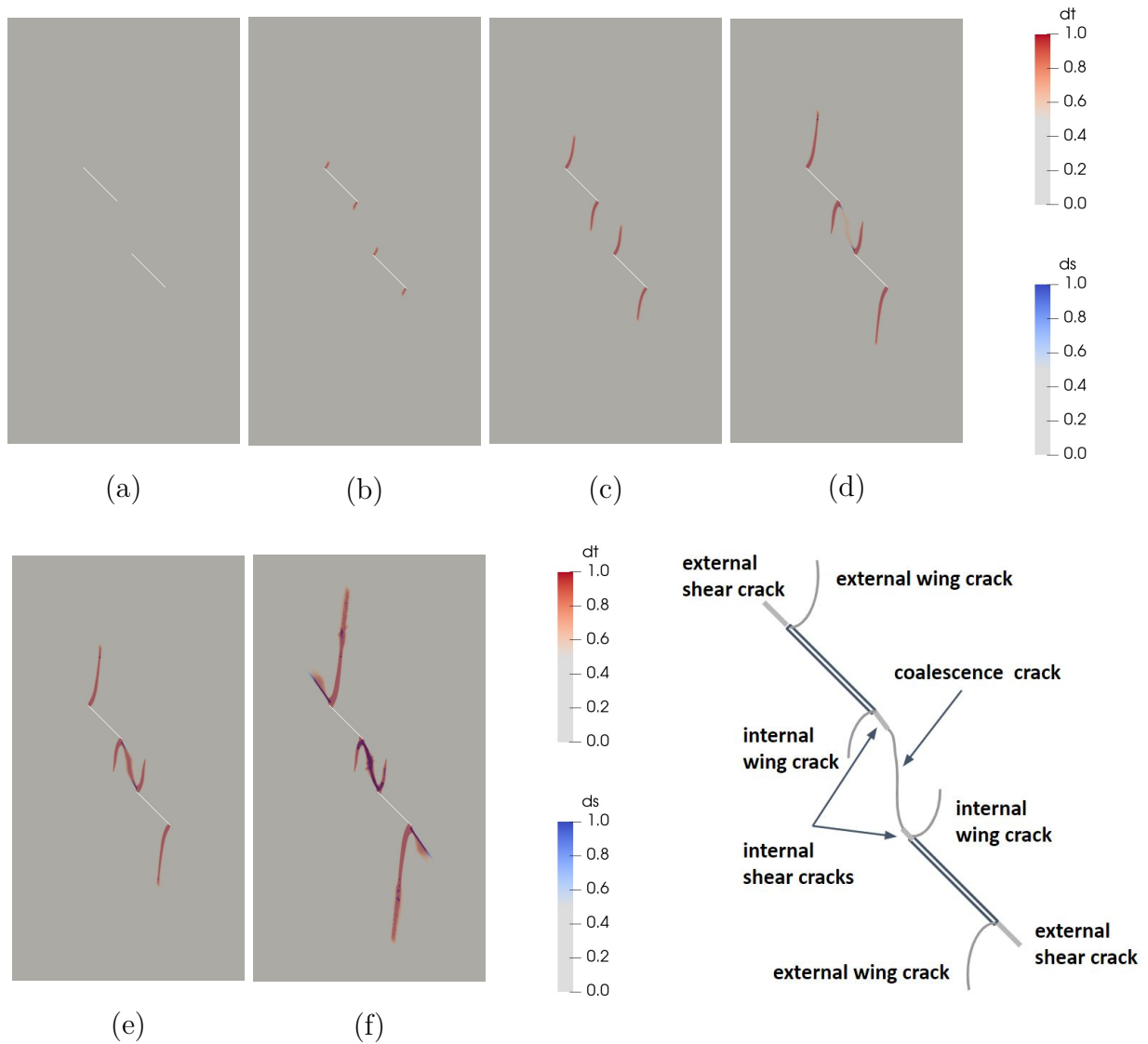


Figure 4: Distribution of tensile and shear damage variable for the case of 45-a-2a at three subsequent values of axial displacement (a)  $u = 0$  mm; (b)  $u = 0.352$  mm; (c)  $u = 0.574$  mm; (d)  $u = 0.620$  mm; (e)  $u = 0.623$  mm; (f)  $u = 0.653$  mm

303 The third configuration of two initial flaws corresponds to “45-2a-2a”. The distributions  
304 of tensile and shear damage obtained are presented in Figure 5 also for three subsequent  
305 values of axial displacement. From step (a) to (b), similarly to the two previous cases, four  
306 tensile wing cracks are created and they propagate toward the compression axis. But from  
307 step (c), the two internal wing cracks have a longer propagation length than the previous  
308 configurations due to the larger spacing between the two initial flaws. At the same time,  
309 four shear cracks are also generated respectively from the ends of initial flaws. When the  
310 prescribed displacement reaches step (f), a coalescence zone is formed by the two internal  
311 wing cracks and two internal shear cracks. Once again, these complex cracking patterns are  
312 well reproduced by the proposed numerical model.

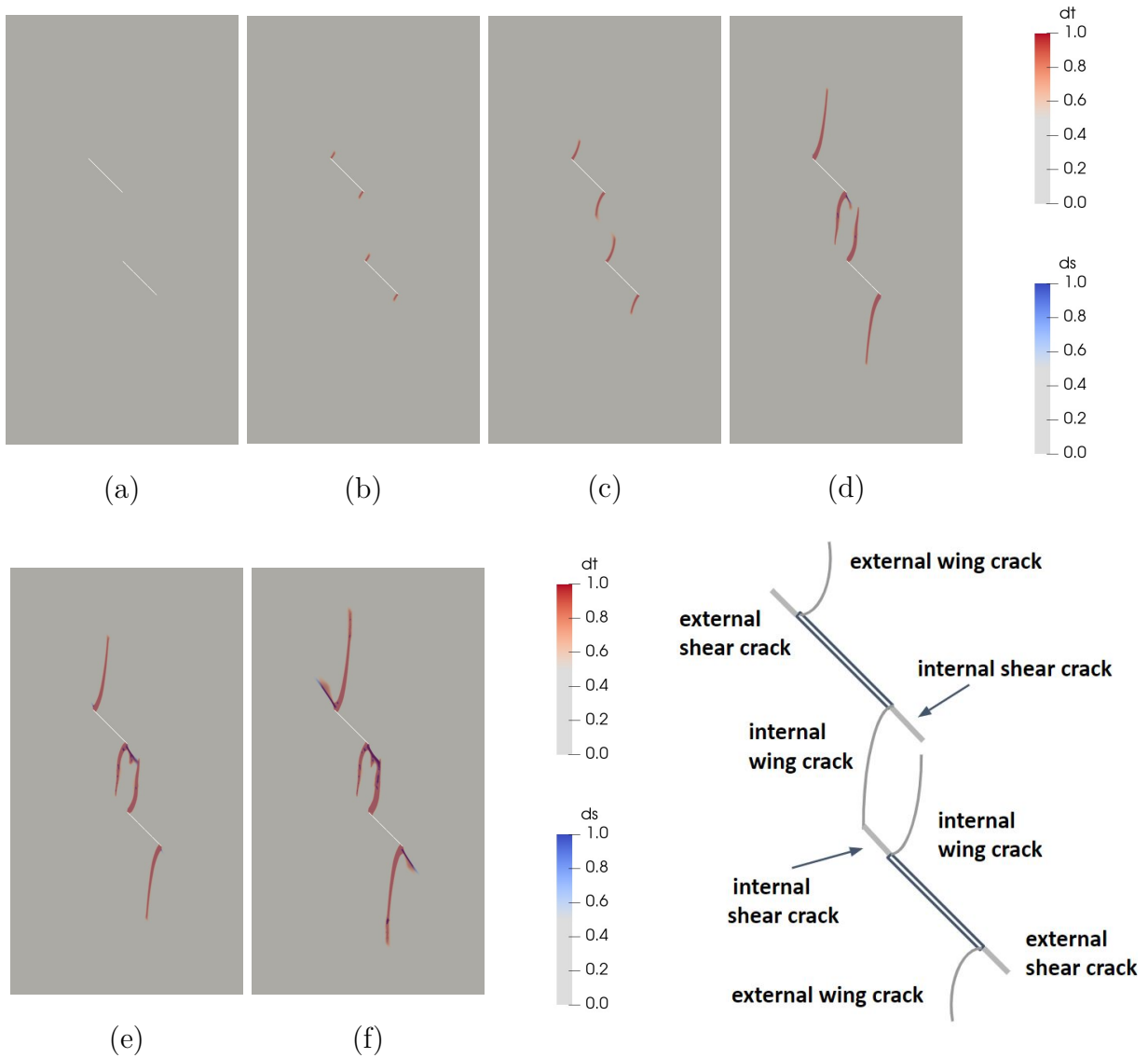


Figure 5: Distributions of tensile and shear damage for the configuration of 45-2a-2a at three subsequent steps of axial displacement (a)  $u = 0$  mm; (b)  $u = 0.370$  mm; (c)  $u = 0.561$  mm; (d)  $u = 0.679$  mm; (e)  $u = 0.685$  mm; (f)  $u = 0.705$  mm

313 In order to compare with the stress value measured from experiment and identify the stat  
 314 of displacement loading in the simulation, the stress-displacement curve is given in Figure  
 315 6. Furthermore, a quantitative comparison between numerical and experimental results is  
 316 provided for all of the three tests. The step (b) of Figure 3, 4 and 5 shows the moment of wing  
 317 crack's onset, and the step (e) shows the one of coalescence crack's onset. Good agreement

318 is achieved from the quantitative comparison for both of wing crack and coalescence crack.  
 319 Moreover, it is clear to see that the onset of wing crack does not affect the linear behavior  
 320 of stress-displacement curves. On the other hand, the onset of coalescence crack between  
 321 two initial flaws directly leads to the reduction of stress. This reasonable feature verifies the  
 322 proposed double phase-field model as well.

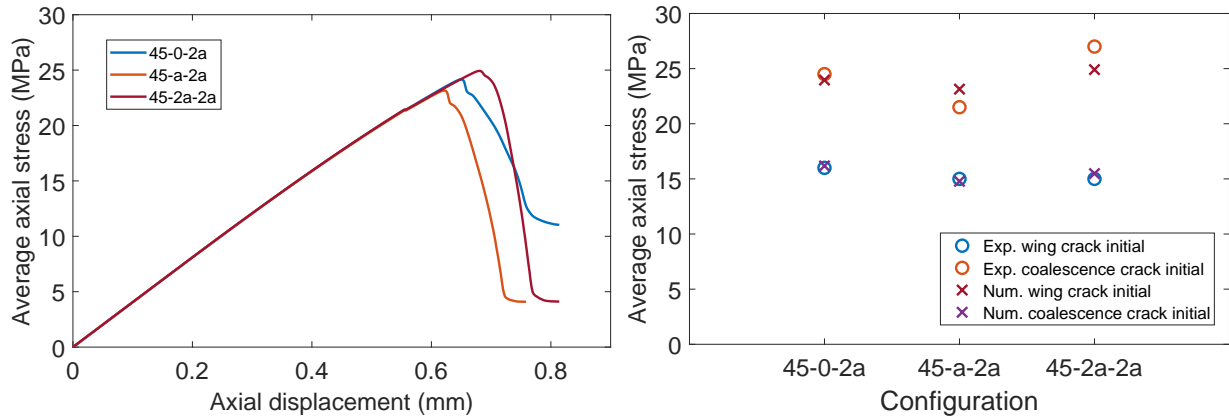


Figure 6: Left: Curves of stress-displacement for numerical test of '45-0-2a', '45-a-2a' and '45-2a-2a'; Right: The comparisons between numerical and experimental results for the wing crack and the coalescence crack initial stress

#### 323 4.2. Bi-axial compression of a plate with two inclined flaws

324 In most previous studies devoted to rock-like materials, only uniaxial compression was  
 325 generally considered. In practice, these materials are subjected to multi-axial stresses. In  
 326 this study, the cracking process is investigated in a plate with two initial flaws subjected to  
 327 bi-axial compression, as shown in Figure 2. Again based on the laboratory tests reported in  
 328 [56, 57], the configuration "45-a-a" is here considered as an example.

329 In Figure 7, the distributions of tensile and shear damage are presented for six different  
 330 values of axial displacement in a bi-axial compression test with a lateral stress of 7.5 MPa. It  
 331 is clear that contrary to the uniaxial compression tests considered above, due to the confining  
 332 effect of lateral stress, the tensile damage is significantly attenuated. The shear cracking  
 333 is the principal mechanism of damage. The shear crack constitutes the bridge linking two  
 334 initial flaws. Two second shear cracks are also observed around the external ends of the

335 initial flaws. The cracking patterns provided by the proposed phase-field method agree well  
 336 with the experimental observations. It seems that the new model is able to describe the  
 337 effect of confining stress on the kinetics of shear cracks commonly observed in rock-like  
 338 materials.

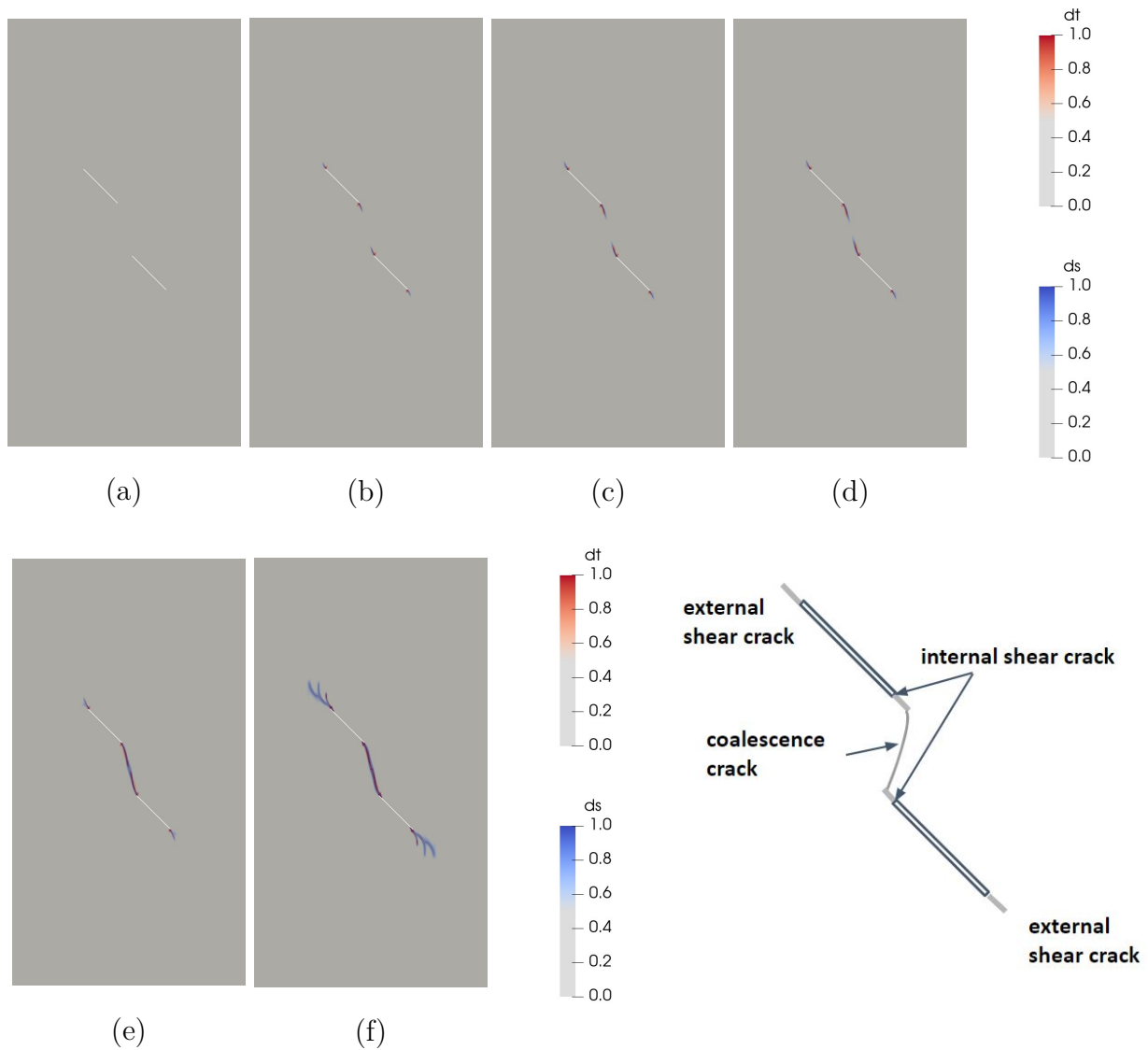


Figure 7: Distribution of tensile and shear damage for the configuration 45-a-a at three values of prescribed axial displacement at (a)  $u = 0$  mm; (b)  $u = 0.793$  mm; (c)  $u = 0.801$  mm; (d)  $u = 0.803$  mm; (e)  $u = 0.809$  mm; (f)  $u = 0.850$  mm, in a bi-axial compression with a lateral stress of  $P_c=7.5$  MPa

339 The stress-displacement curve for the simulation of bi-axial compression is given in Figure



340 8. An obvious difference between the numerical and experimental results if the friction angle  
 341  $\varphi = 30^\circ$  is used as in the uniaxial compression tests. In this way, the friction angle is  
 342 assumed to be increased according to the lateral stress. The simulations by using  $\varphi = 32^\circ$   
 343 and  $34^\circ$  are given. The quantitative stress result is improved while the crack model is not  
 344 changed (compare with figure 7).

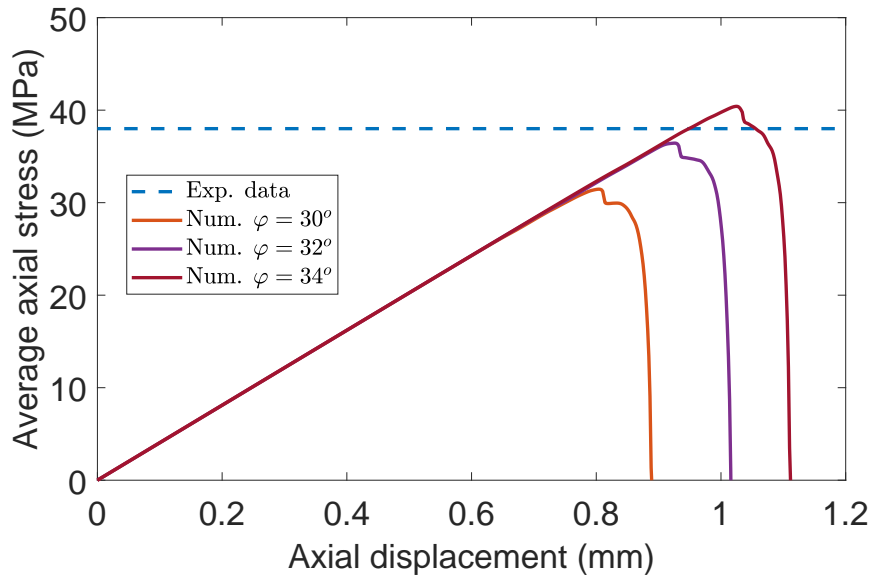


Figure 8: The curves of stress-displacement simulated by using different friction angle  $\varphi = 30^\circ, 32^\circ$  and  $34^\circ$  comparing with the experimental coalescence crack initial stress, in a bi-axial compression with a lateral stress of  $P_c=7.5$  MPa

## 345 5. Discussion

346 The fundamental idea of this double phase-field model is proposed in order to identify  
 347 the mixed crack problem from the in-situ experiment in the context of radioactive waste  
 348 disposal. Since the complex damage zone due to the excavation plays an important role on  
 349 the later thermo-hydrromechanical coupling behavior, the concept of our double phase-field  
 350 model is proposed to distinguish the tensile and compressive-shear damage in [41].

351 Recently, Fei and Choo[30] did a excellent work by using a similar concept of double phase-  
 352 field model. Following their old work[28], they identify the crack condition as: open, stick  
 353 and slip according to the direction of crack interface. The tensile and compressive-shear

354 crack are properly distinguished with the help of the sign of normal stress and slip criterion  
355 of crack. Comparing with the work of Fei and Choo, this work focus on the rock-like  
356 material, so that the Mohr-Coulomb criterion is modified to identify the driving force of  
357 compressive-shear crack. In this way, the further assumptions of friction crack based on  
358 Mohr-Coulomb criterion can be considered in the future study of mixed crack. On the other  
359 hand, the tensile and compressive-shear crack can exist at the same time according to the  
360 degradation of the stiffness matrix with the help of spectral decomposition. Therefore, both  
361 of two double phase-field models work well for the identification of mixed cracks by using  
362 several damage variables, but under different physical assumptions, especially for the friction  
363 crack.

## 364 **6. Conclusion**

365 In this paper, a new phase-field method has been developed for modelling complex crack-  
366 ing modes in rock-like brittle materials subjected to compression-dominating loads. Two  
367 interacting crack fields have been introduced for capturing the tensile and shear crack re-  
368 spectively. The emphasis was put on the description of shear crack growth and propagation  
369 under compressive stresses through a specific Mohr-Coulomb type frictional sliding criterion.  
370 The combination of two crack fields allows modelling mixed cracking patterns. The proposed  
371 method has been implemented in a computer code with the finite element method. It has  
372 been applied to describe complex cracking processes in brittle materials under both uniaxial  
373 and bi-axial compressive stresses. It was found that the new double phase-field method was  
374 able to capture well the main cracking features observed in laboratory tests. **Furthermore,**  
375 **the loading stress state corresponding to the initial wing cracks and coalescence cracks is well**  
376 **reproduced.** Compared with most previous studies, the new phase-field method is able to  
377 well describe the effect of confining stress on the growth of shear cracks commonly observed  
378 in rock-like materials. The proposed method can be easily extended to materials with an  
379 initial anisotropy and to include plastic deformation.

380 **Acknowledgement:**

381 This work has been partially supported by the French National Agency for radioactive  
382 waste management (ANDRA).

383 **References**

- 384 [1] J. Oliver, Modelling strong discontinuities in solid mechanics via strain softening constitutive equations,  
385 part 1: fundamentals, *Internat. J. Numer. Methods Engrg.* 39 (1996) 3575–3600.
- 386 [2] N. Moes, J. Dolbow, T. Belytschko, A finite element method for crack growth without remeshing,  
387 *Internat. J. Numer. Methods Engrg.* 46 (1999) 131–150.
- 388 [3] Q. Zeng, J. Yao, S. JF, Numerical study of hydraulic fracture propagation accounting for rock  
389 anisotropy, *Journal of Petroleum Science and Engineering* 160 (2018) 422–432.
- 390 [4] Q. Zeng, J. Yao, S. JF, Study of hydraulic fracturing in an anisotropic poroelastic medium via a hybrid  
391 edfm-xfem approach, *Computers and Geotechnics* 105 (2019) 51–68.
- 392 [5] N. Moes, C. Stolz, N. Chevaugeon, P. E. Bernard, A level set based model for damage growth: The thick  
393 level set approach, *International Journal for Numerical Methods in Engineering* 86 (2010) 358–380.
- 394 [6] P. E. Bernard, N. Moes, N. Chevaugeon, Damage growth modeling using the thick level set (tls)  
395 approach: Efficient discretization for quasi-static loadings, *Computer Methods in Applied Mechanics  
396 and Engineering* 233-236 (2012) 11–27.
- 397 [7] Q. Zhu, L. Zhao, J. Shao, Analytical and numerical analysis of frictional damage in quasi brittle  
398 materials, *Journal of the Mechanics and Physics of Solids* 92 (2016) 137–163.
- 399 [8] L. Zhao, Q. Zhu, J. Shao, A micromechanics-based plastic damage model for quasi brittle materials  
400 under a large range of compressive stress, *International Journal of Plasticity* 100 (2018) 156–176.
- 401 [9] L. Zhao, J. Shao, Q. Zhu, Analysis of localized cracking in quasi-brittle materials with a micromechanics  
402 based friction damage approach, *Journal of the Mechanics and Physics of Solids* 119 (2018) 163–187.
- 403 [10] G. A. Francfort, J.-J. Marigo, Revisiting brittle fracture as an energy minimization problem, *Journal  
404 of the Mechanics and Physics of Solids* 46 (8) (1998) 1319–1342.
- 405 [11] L. Ambrosio, V. M. Tortorelli, Approximation of functional depending on jumps by elliptic functional  
406 via t-convergence, *Communications on Pure and Applied Mathematics* 43 (8) (1990) 999–1036.
- 407 [12] D. Mumford, J. Shah, Optimal approximations by piecewise smooth functions and associated variational  
408 problems, *Communications on pure and applied mathematics* 42 (5) (1989) 577–685.
- 409 [13] B. Bourdin, G. A. Francfort, J.-J. Marigo, Numerical experiments in revisited brittle fracture, *Journal  
410 of the Mechanics and Physics of Solids* 48 (4) (2000) 797–826.

- 411 [14] C. Miehe, M. Hofacker, F. Welschinger, A phase field model for rate-independent crack propagation:  
412 Robust algorithmic implementation based on operator splits, *Computer Methods in Applied Mechanics*  
413 *and Engineering* 199 (45-48) (2010) 2765–2778.
- 414 [15] M. J. Borden, C. V. Verhoosel, M. A. Scott, T. J. Hughes, C. M. Landis, A phase-field description of  
415 dynamic brittle fracture, *Computer Methods in Applied Mechanics and Engineering* 217 (2012) 77–95.
- 416 [16] M. Ambati, T. Gerasimov, L. De Lorenzis, A review on phase-field models of brittle fracture and a new  
417 fast hybrid formulation, *Computational Mechanics* 55 (2) (2015) 383–405.
- 418 [17] C. Miehe, M. Hofacker, L.-M. Schänzel, F. Aldakheel, Phase field modeling of fracture in multi-physics  
419 problems. part ii. coupled brittle-to-ductile failure criteria and crack propagation in thermo-elastic–  
420 plastic solids, *Computer Methods in Applied Mechanics and Engineering* 294 (2015) 486–522.
- 421 [18] M. J. Borden, T. J. Hughes, C. M. Landis, A. Anvari, I. J. Lee, A phase-field formulation for fracture in  
422 ductile materials: Finite deformation balance law derivation, plastic degradation, and stress triaxiality  
423 effects, *Computer Methods in Applied Mechanics and Engineering* 312 (2016) 130–166.
- 424 [19] J. Choo, W. Sun, Coupled phase-field and plasticity modeling of geological materials: From brittle  
425 fracture to ductile flow, *Computer Methods in Applied Mechanics and Engineering* 330 (2018) 1–32.
- 426 [20] J. Fang, C. Wu, J. Li, Q. Liu, C. Wu, G. Sun, L. Qing, Phase field fracture in elasto-plastic solids:  
427 variational formulation for multi-surface plasticity and effects of plastic yield surfaces and hardening,  
428 *International Journal of Mechanical Sciences* (2019).
- 429 [21] X. Zhang, S. W. Sloan, C. Vignes, D. Sheng, A modification of the phase-field model for mixed mode  
430 crack propagation in rock-like materials, *Computer Methods in Applied Mechanics and Engineering*  
431 322 (2017) 123–136.
- 432 [22] E. C. Bryant, W. Sun, A mixed-mode phase field fracture model in anisotropic rocks with consistent  
433 kinematics, *Computer Methods in Applied Mechanics and Engineering* 342 (2018) 561–584.
- 434 [23] T.-T. Nguyen, J. Rethore, J. Yvonnet, M.-C. Baietto, Multi-phase-field modeling of anisotropic crack  
435 propagation for polycrystalline materials, *Computational Mechanics* 60 (2) (2017) 289–314.
- 436 [24] J. Bleyer, R. Alessi, Phase-field modeling of anisotropic brittle fracture including several damage mech-  
437 anisms, *Computer Methods in Applied Mechanics and Engineering* 336 (2018) 213–236.
- 438 [25] B. Evans, J. T. Fredrich, T.-F. Wong, The brittle-ductile transition in rocks: Recent experimental and  
439 theoretical progress, *The Brittle-Ductile Transition in Rocks, Geophys. Monogr. Ser* 56 (1990) 1–20.
- 440 [26] T.-f. Wong, P. Baud, The brittle-ductile transition in porous rock: A review, *Journal of Structural*  
441 *Geology* 44 (2012) 25–53.
- 442 [27] S. Zhou, X. Zhuang, T. Rabczuk, Phase field modeling of brittle compressive-shear fractures in rock-like  
443 materials: A new driving force and a hybrid formulation, *Computer Methods in Applied Mechanics*  
444 *and Engineering* 355 (2019) 729–752.

- 445 [28] F. Fei, J. Choo, A phase-field method for modeling cracks with frictional contact, *International Journal*  
446 *for Numerical Methods in Engineering* 121 (4) (2020) 740–762.
- 447 [29] A. Palmer, J. Rice, The growth of slip surfaces in the progressive failure of over-consolidated clay,  
448 *Proceedings of the Royal Society of London. A. Mathematical and Physical Sciences* 332 (1591) (1973)  
449 527–548.
- 450 [30] F. Fei, J. Choo, A phase-field model of frictional shear fracture in geologic materials, *Computer Methods*  
451 *in Applied Mechanics and Engineering* 369 (2020) 113265.
- 452 [31] L. Wang, C. Vuik, H. Hajibeygi, A stabilized mixed-fe scheme for frictional contact and shear failure  
453 analyses in deformable fractured media, *Engineering Fracture Mechanics* 267 (2022) 108427.
- 454 [32] A. Spetz, R. Denzer, E. Tudisco, O. Dahlblom, A modified phase-field fracture model for simulation  
455 of mixed mode brittle fractures and compressive cracks in porous rock, *Rock Mechanics and Rock*  
456 *Engineering* 54 (2021) 1–14.
- 457 [33] Q. Wang, Y. Feng, W. Zhou, Y. Cheng, G. Ma, A phase-field model for mixed-mode fracture based  
458 on a unified tensile fracture criterion, *Computer Methods in Applied Mechanics and Engineering* 370  
459 (2020) 113270.
- 460 [34] J. Ulloa, J. Wambacq, R. Alessi, E. Samaniego, G. Degrande, S. François, A micromechanics-  
461 based variational phase-field model for fracture in geomaterials with brittle-tensile and compressive-  
462 ductile behavior, *Journal of the Mechanics and Physics of Solids* 159 (2022) 104684.
- 463 [35] T. You, H. Waisman, Q.-Z. Zhu, Brittle-ductile failure transition in geomaterials modeled by a modified  
464 phase-field method with a varying damage-driving energy coefficient, *International Journal of Plasticity*  
465 136 (2021) 102836.
- 466 [36] K. Oshima, T. Takaki, M. Muramatsu, Development of multi-phase-field crack model for crack prop-  
467 agation in polycrystal, *International Journal of Computational Materials Science and Engineering* 03  
468 (2014) 1450009.
- 469 [37] T.-T. Nguyen, J. Réthoré, J. Yvonnet, M.-C. Baietto, Multi-phase-field modeling of anisotropic crack  
470 propagation for polycrystalline materials, *Computational Mechanics* 60 (2017) 289–314.
- 471 [38] S. Na, W. Sun, Computational thermomechanics of crystalline rock, part i: A combined multi-phase-  
472 field/crystal plasticity approach for single crystal simulations, *Computer Methods in Applied Mechanics*  
473 *and Engineering* 338 (2018) 657–691.
- 474 [39] A. Dean, P. Asur Vijaya Kumar, J. Reinoso, C. Gerendt, M. Paggi, E. Mahdi, R. Rolfes, A multi  
475 phase-field fracture model for long fiber reinforced composites based on the pucker theory of failure,  
476 *Composite Structures* 251 (2020) 112446.
- 477 [40] J. Bleyer, R. Alessi, Phase-field modeling of anisotropic brittle fracture including several damage mech-  
478 anisms, *Computer Methods in Applied Mechanics and Engineering* 336 (2018) 213–236.

- 479 [41] Z. Yu, J. F. Shao, M. N. Vu, G. Armand, Numerical study of thermo-hydro-mechanical responses of in  
480 situ heating test with phase-field model., *International Journal of Rock Mechanics and Mining Sciences*  
481 138 (2021) 104542.
- 482 [42] F. Fei, J. Choo, Double-phase-field formulation for mixed-mode fracture in rocks, *Computer Methods*  
483 *in Applied Mechanics and Engineering* 376 (2021) 113655.
- 484 [43] T. F. Wong, Micromechanics of faulting in westerly granite, in: *International journal of rock mechanics*  
485 *and mining sciences & geomechanics abstracts*, Vol. 19, Elsevier, 1982, pp. 49–64.
- 486 [44] R. Wong, K. Chau, C. Tang, P. Lin, Analysis of crack coalescence in rock-like materials containing three  
487 flaws—part i: experimental approach, *International Journal of Rock Mechanics and Mining Sciences*  
488 38 (7) (2001) 909–924.
- 489 [45] M. S. Paterson, T.-f. Wong, *Experimental rock deformation—the brittle field*, Springer Science & Busi-  
490 ness Media, 2005.
- 491 [46] V. Lubarda, D. Krajcinovic, S. Mastilovic, Damage model for brittle elastic solids with unequal tensile  
492 and compressive strengths, *Engineering Fracture Mechanics* 49 (5) (1994) 681–697.
- 493 [47] S. Murakami, *Continuum damage mechanics: a continuum mechanics approach to the analysis of*  
494 *damage and fracture*, Vol. 185, Springer Science & Business Media, 2012.
- 495 [48] C. Miehe, Comparison of two algorithms for the computation of fourth-order isotropic tensor functions,  
496 *Computers & structures* 66 (1) (1998) 37–43.
- 497 [49] C. Miehe, M. Lambrecht, Algorithms for computation of stresses and elasticity moduli in terms of  
498 seth–hill’s family of generalized strain tensors, *Communications in numerical methods in engineering*  
499 17 (5) (2001) 337–353.
- 500 [50] S. Zhang, W. Jiang, M. R. Tonks, A new phase field fracture model for brittle materials that accounts  
501 for elastic anisotropy, *Computer Methods in Applied Mechanics and Engineering* 358 (2020) 112643.
- 502 [51] T. T. Nguyen, J. Yvonnet, Q.-Z. Zhu, M. Bornert, C. Chateau, A phase-field method for computational  
503 modeling of interfacial damage interacting with crack propagation in realistic microstructures obtained  
504 by microtomography, *Computer Methods in Applied Mechanics and Engineering* 312 (2016) 567–595.
- 505 [52] J. Y. Wu, V. P. Nguyen, C. T. Nguyen, D. Sutula, S. Bordas, S. Sinaie, B. S. P. A, Chapter one -  
506 phase field modeling of fracture, *Advances in Applied Mechancis* 53 (2020) 1–183.
- 507 [53] Z. Li, Q.-h. Zhu, B.-l. Tian, T.-f. Sun, D.-w. Yang, A damage model for hard rock under stress-induced  
508 failure mode, in: *Advanced Engineering and Technology III: Proceedings of the 3rd Annual Congress*  
509 *on Advanced Engineering and Technology (CAET 2016)*, Hong Kong, 22-23 October 2016, CRC Press,  
510 2017, p. 87.
- 511 [54] C. Miehe, F. Welschinger, M. Hofacker, Thermodynamically consistent phase-field models of fracture:  
512 variational principles and multi-field fe implementations, *International Journal for Numerical Methods*

- 513 in Engineering 83 (10) (2010) 1273–1311.
- 514 [55] B. Bourdin, G. A. Francfort, J.-J. Marigo, The variational approach to fracture, Journal of elasticity  
515 91 (1-3) (2008) 5–148.
- 516 [56] A. Bobet, Fracture coalescence in rock materials: Experimental observations and numerical predictions.,  
517 Ph.D. thesis, Massachusetts Institute of Technology (1998).
- 518 [57] A. Bobet, H. H. Einstein, Numerical modeling of fracture coalescence in a model rock material, Inter-  
519 national Journal of Fracture 92 (3) (1998) 221.
- 520 [58] H. Amor, J.-J. Marigo, C. Maurini, Regularized formulation of the variational brittle fracture with  
521 unilateral contact: Numerical experiments, Journal of the Mechanics and Physics of Solids 57 (8)  
522 (2009) 1209–1229.